Volume 53
Number 28
28 July 2024
Pages 11587-12008

Dalton Transactions

An international journal of inorganic chemistry

rsc.li/dalton

ISSN 1477-9226

ROYAL SOCIETY OF CHEMISTRY

PAPER

Keiichi Katoh *et al.*

Spin dynamics phenomena of a cerium(III) double-decker complex induced by intramolecular electron transfer

Dalton Transactions

ROYAL SOCIETY OF CHEMISTRY

PAPER

View Article Online
View Journal | View Issue

Cite this: *Dalton Trans.*, 2024, **53**, 11664

Spin dynamics phenomena of a cerium(III) double-decker complex induced by intramolecular electron transfer†

Kana Kobayashi,[a] Michiyuki Suzuki,[a] Tetsu Sato,[a] Yoji Horii,[b] Takefumi Yoshida,[c] Brian. K. Breedlove,[a] Masahiro Yamashita [a,d] and Keiichi Katoh *[e]

Received 15th February 2024,
Accepted 17th April 2024

DOI: 10.1039/d4dt00436a

rsc.li/dalton

Switchable spin dynamic properties in single-molecule magnets (SMMs) *via* an applied stimulus have applications in single-molecule devices. Many SMMs containing heavy lanthanoid ions with strong uniaxial magnetic anisotropy have been reported to exhibit SMM characteristics in the absence of an external magnetic field. On the other hand, SMMs containing light lanthanoid cerium(III) (Ce^{3+}) ions exhibit field-induced slow magnetic relaxation. We investigated the chemical conversion of a diamagnetic Ce^{4+} ion ($4f^0$) to a paramagnetic Ce^{3+} ion ($4f^1$) in Ce-phthalocyaninato double-decker complexes ($TBA^+[Ce(obPc)_2]^-$ (**1**) and $TBA^+[Ce(Pc)_2]^-$ (**2**)) which exhibit field-induced SMM behaviour due to a $4f^1$ system. The phthalocyaninato ligands with electron-donating substituents ($obPc^{2-}$ = 2,3,9,10,16,17,23,24-octabutoxyphthalocyaninato) in **1** have a significant effect on the valence state of the Ce ion, which is reflected in its magnetic properties due to the mixed valence state of the Ce ion. Given that Ce double-decker complexes with π-conjugated ligands undergo intramolecular electron transfer (IET) to the Ce ion mixed valence state, characterised by a mixture of $4f^0$ and $4f^1$ configurations, we examined the dynamic disorder inherent in IET influencing magnetic relaxation.

Introduction

Single-molecule magnets (SMMs) are possible candidates for bits in ultra-high-density memory devices and qubits in quantum computers (QC).[1–3] SMMs are basically 'single domain magnets' since the magnetic interactions between molecules can be ignored due to the fixed number of metal ions and well-ordered magnetic structures.[4] Furthermore, SMMs show slow magnetic relaxation rates and quantum tunnelling of the magnetisation (QTM) in a single molecule due to the nature of the electronic structures, which is different from bulk magnets. To make SMMs practical for QC and quantum information processing (QIP),[5,6] the energy barrier for spin reversal (U_{eff}) and fast QTM processes must be controlled.[6–9] In crystals, the degenerate orbitals of d and f electrons forming the electronic states reflect the ligand field (LF). As a result, the LF directly influences the uniaxial magnetic anisotropy. Several groups have recently reported the rational molecular design of lanthanoid(III) (Ln^{3+})-based SMMs, which have distinctive features, including slow magnetic relaxation and QTM.[11–18] Although many articles and reviews show that molecular design is essential for SMM behaviour, controlling the magnetic relaxation pathway is still challenging.[19–22]

Since SMM properties are rooted in large uniaxial magnetic anisotropies, it is effective to use heavy Ln^{3+} ions, such as Tb^{3+}, Dy^{3+}, and Er^{3+} ions, for high-performance SMMs.[23] However, cerium(III) (Ce^{3+}) SMMs with a $4f^1$ electron configuration have been reported.[24–40] In 2013, Kajiwara and co-workers pointed out that the shape of the charge density distribution of a Ce^{3+} ion was oblate, which is the same as those of Tb^{3+} ($4f^8$) and Dy^{3+} ($4f^9$) ions.[17,24,41] Therefore, the total angular momentum J in the axial direction of the main axis of the Ce^{3+} ion is stabilised in the axial LF, and SMM behaviour occurs. In the Ce^{3+} ion ground state of $J = 5/2$, 6 (= $2J + 1$) levels are degenerate ($^2F_{5/2}$, $S = 1/2$, $L = 3$, $J = 5/2$, $g_J = 6/7$), and the energy is split by adding an LF, meaning a Kramers doublet

[a]*Department of Chemistry, Graduate School of Science, Tohoku University, 6-3, Aramaki-Aza-Aoba, Aoba-ku, Sendai, Miyagi 980-8578, Japan*
[b]*Department of Chemistry, Faculty of Science, Nara Women's University, Kitauoya Higashimachi, Nara 630-8506, Japan*
[c]*Cluster of Nanomaterials, Graduate School of Systems Engineering, Wakayama University, 930 Sakae-Dani, Wakayama, 640-8510, Japan*
[d]*School of Chemical Science and Engineering, Tongji University, Siping Road 1239, Shanghai 200092, P. R. China*
[e]*Department of Chemistry, Graduate School of Science, Josai University, 1-1, Keyakidai, Sakaddo, Saitama 350-0295, Japan. E-mail: kkatoh@josai.ac.jp*

†Electronic supplementary information (ESI) available. CCDC 2332889 for Ce(obPc)$_2$ and 2332908 for **1**. For ESI and crystallographic data in CIF or other electronic format see DOI: https://doi.org/10.1039/d4dt00436a

(KD) structure remains. However, whether the KD term ($|M_J|$ = 5/2, 3/2, and 1/2) has the lowest energy depends on the LF. Ce^{3+} complexes have an energy gap between the ground state and the first excited state, which has been reported to be *ca.* 20 cm^{-1} and are wide enough to prevent spin reversal.[24–40] However, the magnetic relaxation of Ce^{3+} type SMMs occurs *via* a Raman process below 10 K.[35,42,43] The spin state of the $4f^1$ electron is the origin of the slow magnetic relaxation phenomenon. In addition, since the stable isotopes of Ce (isotopic nuclides ^{140}Ce, ^{142}Ce, ^{138}Ce, and ^{136}Ce) have no nuclear spin, investigating the magnetic relaxation phenomena, including the ground state and excited state, will provide important insights into the molecular design of Ce-based SMMs.[44,45]

In Ce compounds with sandwich structures, like cerocene and phthalocyaninato multiple-decker complexes, where Ce is sandwiched by π-conjugated ligands, the valence state of the Ce ion may be in an intermediate electronic state between trivalent (Ce^{3+}) and tetravalent (Ce^{4+}).[25,46–48] Precise determination of the valence state of Ce ions in a mixed valence state has been attempted using various methods, including X-ray absorption near edge structure (XANES) and cyclic voltammetry (CV).[48–50] However, the determination of the valence state of a Ce ion still has many uncertainties, and it has been reported that its valence state can change depending on the influence of the substituents attached to the ligands.

From the viewpoint of magnetic switching properties, the total angular momentum of Ce^{3+} ions is J = 5/2, and Ce^{3+} compounds are paramagnetic with a $4f^1$ configuration. On the other hand, the total angular momentum of Ce^{4+} ions with a $4f^0$ configuration is J = 0, making it diamagnetic. In this sense, Ce^{4+}-phthalocyaninato (Pc^{2-}) double-decker complexes (Ce$(Pc)_2$) are best suited for magnetic switching since $Ce^{4+}(4f^0) \rightleftharpoons Ce^{3+}(4f^1)$ occurs easily (Fig. 1). We studied the Ce^{3+} ion ($4f^1$) spin dynamics *via* an intramolecular electron transfer (IET) between the Ce^{3+} ion and the Pc ligands of Ce–Pc double-decker complexes ($TBA^+[Ce(obPc)_2]^-$ (**1**) and $TBA^+[Ce(Pc)_2]^-$ (**2**)) (TBA^+ = tetrabutylammonium, $obPc^{2-}$ = 2,3,9,10,16,17,23,24-octabutoxyphthalocyaninato, Pc^{2-} = phthalocyaninato). Moreover, we focused on the effects of IET on the magnetic relaxation process due to the dynamic disorder of the molecular structures.

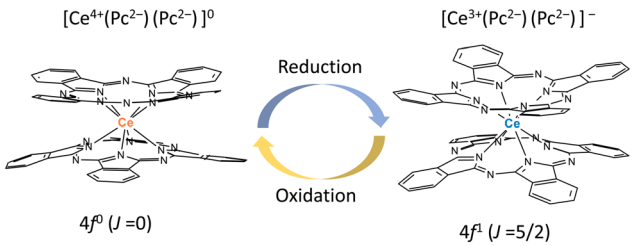

Fig. 1 Schematic illustration of redox-active Ce^{4+}-phthalocyaninato double-decker complex $Ce(Pc)_2$, which has magnetic switching due to ease of reduction/oxidation of the Ce ion.

Experimental

All reagents were purchased from Wako Pure Chemical Industries, Ltd, TCI, Strem Chemicals, Inc., and Sigma-Aldrich Co. LLC and used without further purification. Complexes **1** and **2** were prepared according to previously reported literature procedures.[48,51–53]

Synthesis of $TBA^+[Ce(obPc)_2]^-$ (1)

Neutral $Ce(obPc)_2$ was synthesised as follows. $Ce(OAc)_3{\cdot}H_2O$ (335 mg, 1.0 mmol), and 1,8-diazabicyclo[5,4,0]undec-7-ene (DBU) (1 mL) and 4,5-dibutoxyphthalonitrile (2125 mg, 7.8 mmol) were added to 1-hexanol (20 mL). The solution was refluxed under argon for 24 h. After cooling, the obtained solid was purified by using column chromatography (C-200 silica gel, Wako) with chloroform ($CHCl_3$) as the eluent. The cerium double-decker complex $Ce(obPc)_2$ ($obPc^{2-}$ = 2,3,9,10,16,17,23,24-octabutoxyphthalocyaninato) was obtained from the dark green band by removing the solvent. Green needle-like crystals of $Ce(obPc)_2$ were obtained recrystallised by layering a dichloromethane solution with *n*-hexane (964 mg, 0.41 mmol, yield 41%). Single crystals suitable for X-ray diffraction analysis were obtained by diffusing ethanol into a chloroform solution. ESI-MS: *m*/*z*: 2318.07 $[M]^+$ (calcd 2318.90) Anal. calcd (%) for $C_{128}H_{160}N_{16}O_{16}Ce$: C; 66.30, H; 6.96, N; 9.66 found. C; 66.30, H; 6.89, N; 9.62.

The reduced cerium(III) double-decker complex $TBA^+[Ce(obPc)_2]^-$ (**1**) (TBA^+ = tetrabutylammonium) was prepared by adding $Ce(obPc)_2$ (82 mg, 0.035 mmol) and 1.6 mL of hydrazine monohydrate ($N_2H_4{\cdot}H_2O$) to 16 mL of dimethyl sulfoxide (DMSO), heating to boiling with a heat gun, and sonicating for 30 min until the neutral form green completely disappeared, resulting in the solution turning blue, which is the colour of anionic $[Ce(obPc)_2]^-$. Since the redox potential of the Ce^{4+}/Ce^{3+} couple is higher than the redox potential of $N_2H_4{\cdot}H_2O$, Ce^{4+} ions can be reduced to Ce^{3+} ions with $N_2H_4{\cdot}H_2O$. Tetrabutylammonium bromide (TBA·Br) (500 mg) dissolved in 5.0 mL of DMSO was added to the above solution; upon slow diffusion, a light blue solid precipitated out. A light blue solid of **1** was obtained (67 mg, 0.026 mmol, yield 75%). MALDI-MS: *m*/*z*: 2318.12 $[M]^+$ (calcd 2318.90) Anal. Calcd (%) for: $C_{144}H_{196}N_{17}O_{16}Ce{\cdot}H_2O$: C; 67.05, H; 7.74, N; 9.23 found. C; 66.97, H; 7.74, N; 9.20.

The following was performed to obtain a single crystal. A mixture of $Ce(obPc)_2$ (0.78 mg), DMSO (0.58 mL), and $N_2H_4{\cdot}H_2O$ (0.02 mL) was heated at 120 °C for 1 h, affording a blue solution of the anionic double-decker complex ($[Ce(obPc)_2]^-$). After cooling to room temperature, the undissolved solids were removed using a membrane filter. Slow diffusion of the anionic double-decker solution into a DMSO solution of TBA·Br (0.4 M) afforded plate-like crystals of **1**.

Synthesis of $TBA^+[Ce(Pc)_2]^-$ (2)

$Ce(Pc)_2$ was synthesized using the method reported in ref. 53:

"A mixture of 1,2-dicyanobenzene (2150 mg, 16.8 mmol), $Ce(NH_4)_2(NO_3)_6$ (500 mg, 0.912 mmol), and DBU (1.5 mL) in

150 mL of 1-hexanol was refluxed for 20 h. The solution was allowed to cool to room temperature and then filtered. The precipitate was washed with $CHCl_3$ and then dried in the air. The crude purple product was extracted with ten 200 mL portions of $CHCl_3$. The green extracts were combined, concentrated, and purified using column chromatography (C-200 silica gel, Wako) with $CHCl_3$ as the eluent. The green fraction, which was the first fraction, was collected while being careful not to contaminate with the H_2Pc. The green fraction was concentrated, and *n*-hexane was added until the compound precipitated (600 mg, 0.515 mmol, 57%). Deep green needle-like crystals were obtained by diffusing *n*-hexane into a chloroform solution. ESI-MS: *m*/*z* 1164.20 $[M^+]$ (calcd.1164.21)".[53]

The cerium(III) double-decker complex $TBA^+[Ce(Pc)_2]^-$ (**2**) was prepared by adding $Ce(Pc)_2$ (78 mg, 0.067 mmol) and 1.2 mL of $N_2H_4{\cdot}H_2O$ to 30 mL of DMSO, heating to boiling with a heat gun, and sonicating for 30 min until the green neutral form completely disappeared to afford a blue solution, which is the colour of the anionic form $[Ce(Pc)_2]^-$. TBA·Br (600 mg) was added to the above solution, and then the solution was heated with a heat gun and sonicated for 30 min. After adding 300 mL of distilled water and leaving it overnight, the resulting blue solid of **2** was collected by using suction filtration and recrystallised by liquid–liquid diffusion using acetone/*n*-hexane to obtain a purple block-like crystalline solid (73.5 mg, 0.0522 mmol, yield 78%). Elemental analysis calcd (%) for $C_{80}H_{68}N_{17}Ce$: C 68.26, H 4.87, N 16.92; found: C 67.63, H 4.87, N 16.59.

X-ray crystal structure analysis

A single crystal was mounted on a loop rod coated with Paratone-N (HAMPTON RESEARCH). Data were collected on a Rigaku Saturn 724+ CCD diffractometer with graphite monochromated Mo κα radiation (λ = 0.71075 Å) at T = 233 ± 2 K for **1** and T = 100 ± 2 K for **2**. An empirical absorption correction based on azimuthal scans of several reflections was applied. The data were corrected for Lorentz and polarization effects. All non-hydrogen atoms were refined anisotropically using a least-squares method, and hydrogen atoms were fixed at calculated positions and refined using a riding model. SHELXL (2014/7 and 2018/3) was used for structure refinement, and the structure was expanded using Fourier techniques.

Powder X-ray diffraction (PXRD) patterns of crushed polycrystalline samples of **1** were acquired using Bruker X-ray diffractometer (D2 PHASER) operated at 30 kV and 10 mA using a low-background sample holder in the diffraction angle (2θ) range of 3°–60° in steps of 0.02° at 1 s per step. PXRD patterns for crushed crystalline samples of **2** loaded into capillaries (diameter: 0.8 mm, length: 80 mm, Hilgenderg) with the mother liquor were collected at 298 K using a Rigaku X-ray diffractometer (AFC-7R/LW) operated at 50 kV and 300 mA in the 2θ range of 3°–60° in steps of 0.02° and at 2 s per step. Visualization and analysis of the crystal structure and PXRD patterns were simulated from the single crystal data by using Mercury 4.0.

Physical property measurements

Electrospray ionization mass spectroscopy and elemental analyses were performed at the Research and Analytical Centre for Giant Molecules, Tohoku University. Ultraviolet–visible-near infrared (UV-vis-NIR) spectra for chloroform solutions were acquired on a JASCO V-670 spectrophotometer in a quartz cell with a pathlength of 1 cm at 298 K. Infrared (IR) spectra were acquired on a JASCO FT/IR-6600 and FT/IR-6100V in a KBr matrix at 298 K.

Electrochemistry (cyclic voltammetry (CV) and differential pulse voltammetry (DPV)) was performed using an ALS/HCH Model 620D electrochemical analyser. A 0.1 M TBA·PF_6 (tetrabutylammonium hexafluorophosphate) dichloromethane solution was used as the supporting electrolyte. A glassy carbon (3 mm diameter) electrode was used as a working electrode, Pt wire was used as a counter electrode, and Ag/AgCl was used as a reference electrode.

X-ray absorption fine structure (XAFS) measurements were conducted on sample pellets (4 mmϕ) in the BL9A beamline of the Photon Factory (2.5 GeV, 450 mA), operated by the High Energy Accelerator Research Organization (KEK), under proposals 2017P016 and 2019G117. The X-rays were monochromatized with a Si(111) water-cooled double crystal monochromator (resolution: $\Delta E/E \approx 2 \times 10^{-4}$ (9 keV)). A Ni-coated double flat mirror was used to reduce the higher harmonics. Chromium foil was employed to calibrate the Ce L_{III}-edge. The XAFS data was processed using the ATHENA program.[54] Deconvolution analysis of XANES spectrum was performed based on the literature.[55,56]

Magnetic susceptibility measurements were performed on Quantum Design SQUID magnetometers MPMS-XL, MPMS-3, and PPMS ACMS system. Direct current (dc) measurements were performed in the temperature (T) range of 1.8–300 K and dc magnetic fields (H) of −70 to 70 kOe. Alternating current (ac) measurements were performed in the ac frequency (ν) range of 1–1000 Hz with an ac field amplitude of 3 Oe in the presence of an H for **1** (zero to 3 kOe) and **2** (zero to 16 kOe) and the ν range of 10–10 000 Hz with an ac field amplitude of 3 Oe in the presence of a dc field 750 Oe for **2** by using an ACMS. Measurements were performed on randomly oriented powder samples, placed in gel capsules and fixed with *n*-eicosane to prevent them from moving during measurements. Using Pascal's constants, all data were corrected for the sample holder, *n*-eicosane, and diamagnetic contributions from the molecules.

Theoretical calculations

Calculations using a complete active space self-consistent field (CASSCF) method with spin–orbit (SO) coupling (CASSCF-SO) were performed using the ORCA 5.0.3[57] program with the basis set SARC2-DKH-QZVP[58] for the Ce ion, SARC-DKH-TZVP[59] for N donor atoms, and DKH-def2-SVP[59] for non-coordinating atoms. The molecular geometry of the $[Ce(Pc)_2]^-$ unit was taken from the crystal structure and used for the calculations without geometry optimization. For the

calculations on $[Ce(obPc)_2]^-$, the butoxy groups were replaced with methoxy groups to reduce the computational costs. The positions of the methoxy protons were optimized at the B3LYP-D3BJ/Def2-SVP level[60–62] using Y as the metal centre. Seven of the doublet states were mixed with SO coupling. The number of the doublet states corresponds to the number of cases where one electron is present in any of the seven f orbitals. The SINGLE_ANISO module was used to convert the CASSCF-SO results into the wavefunctions in terms of M_J and to calculate the transition magnetic moment among the ligand field sublevels.

Results and discussion

Structural characterisations

The characteristics of SMMs are related to their crystal structures, and the coordination environment of the metal centre is particularly important. Therefore, we analysed the crystal structures of **1** and **2** (Fig. 2 and 3). In Fig. 2, the structures of the neutral (a and c) and reduced complexes (b and d) were significantly different due to the Ce ionic radius (trivalent: 1.14 Å and tetravalent: 0.96 Å). The structures of neutral complexes are shown in Fig. S1 and S3.† In addition, the ionic radius of the Ce ion in $Ce(Pc)_2$ is intermediate between those of Ce^{3+} and Ce^{4+} ions (1.01 Å).[63,64]

Complex **1** has a butoxy group in the $Ce(obPc)_2$ unit and a butyl group in the counter ion TBA^+, and the alkyl chains should be disordered around room temperature. Initially, we obtained the diffraction pattern at 120 K but could not obtain enough reflection spots for structural analysis. Therefore, when we compared the lattice constants at 253 K (a = 33.8093, b = 11.2719, c = 36.7273, α = 90.0000, β = 95.3320, γ = 90.0000) and 120 K (a = 34.8002, b = 11.2341, c = 69.9285, α = 90.0000, β = 96.3154, γ = 90.0000), we found that the c-axis was about twice as long at 120 K, and we could confirm a decrease in symmetry. Since we were able to obtain sufficient reflection spots at 233 K, we performed structural analysis and found that **1** was in the monoclinic space group $I2/a$, and the alkyl chains of $[Ce(obPc)_2]^-$ unit and TBA^+ unit were disordered (Fig. S2 and Table S1†). The presence of the butoxy groups of the $[Ce(obPc)_2]^-$ unit causes the Pc ligand to have a signifi-

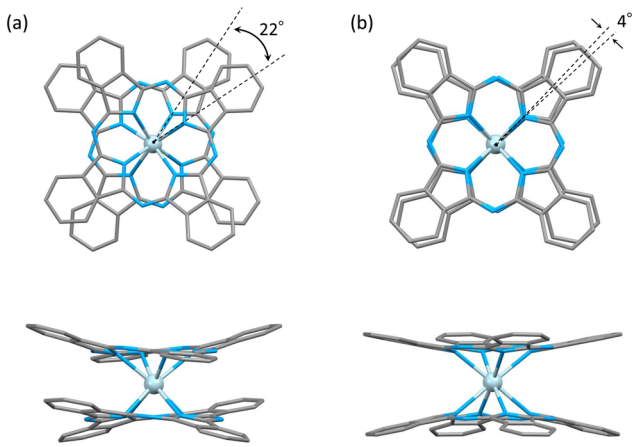

Fig. 3 Crystal structure of Ce–Pc double-decker complexes (a) **1** and (b) **2**: (top) top view and (bottom) side view. *n*-Butoxy substituents, H atom, and tetrabutylammonium in complexes were omitted for clarity. Ce^{3+}: light blue, C: grey, and N: blue.

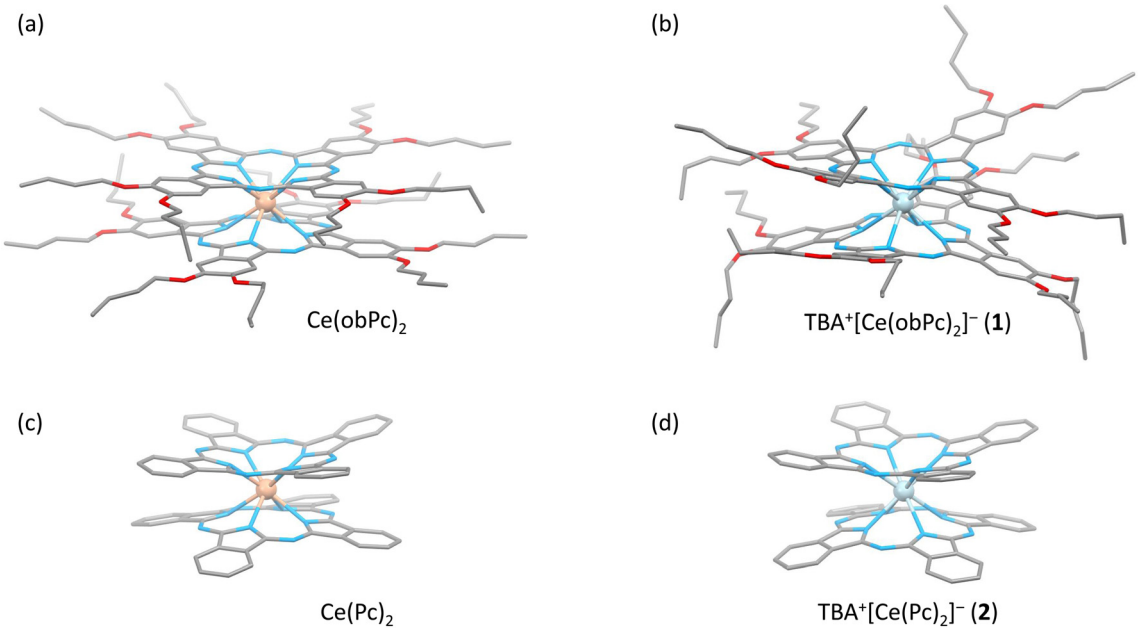

Fig. 2 Molecular structure of Ce-double-decker complexes which is neutral forms (a and c) and reduced forms (b and d) discussed in the main text. The molecular structure of these complexes changes significantly before and after reduction. Ce^{4+}: light orange, Ce^{3+}: light blue, C: grey, N: blue and O: red. H atom and tetrabutylammonium (TBA^+) in complexes were omitted for clarity. See the main text and SI for structural information.

cantly distorted structure, such as saddle-shaped distortion. The stacking angle (φ) between the two Pc^{2-} ligands was determined to be *ca.* 22° (Fig. 3a). Thus, the Ce^{3+} sites in **1** have distorted SP or SAP geometries. The Ce^{3+} ions are spaced between the two Pc^{2-} ligands with distances of 3.16 Å from the mean plane of the four N_{iso} of the two Pc^{2-} ligands. Crystal-packing diagrams of **1** are shown in Fig. S2.† The intermolecular Ce···Ce distance along the *b* axis was determined to be 11.3 Å, and Ce···Ce distance along the *a* and *c* axes were determined to be over 16.9 Å. Each molecule of **1** along the *b* axis is rather well separated from neighbouring molecules due to the alkyl chains of the $[Ce(obPc)_2]^-$ unit and TBA^+ counter ion. However, the structure from the microcrystalline PXRD data at 293 K and simulated from X-ray single crystallographic data at 253 K for **1** almost overlap. At the same time, some polymorphs are present due to the temperature dependence of the diffraction pattern (Fig. S3†).

Complex **2**, shown in Fig. 3b, crystallized in the tetragonal space group *P*4/*ncc*. It has a square prismatic (SP, quasi-D_{4h}) coordination environment, which is the same structure previously reported by Hückstädt *et al.* (Table S2,† CCDC 148306).[52] **2** has a Ce^{3+} ion between two Pc^{2-} ligands and is coordinated with TBA^+ as a counter ion. φ between the two Pc^{2-} ligands was determined to be *ca.* 4°. Thus, the Ce^{3+} site in **2** has a slightly distorted SP geometry. The Ce^{3+} ion is spaced between the two Pc^{2-} ligands with distances of 3.16 Å from the mean plane of the four N_{iso} of the two Pc^{2-} ligands. Crystal-packing diagrams of **2** are shown in Fig. S5.† The intermolecular Ce···Ce distances along the *a* and *c* axes were determined to be 12.13 and 11.24 Å, respectively. Each molecule of **2** along the *c* axis is rather well separated from neighbouring molecules due to the TBA^+ counter ion. Furthermore, PXRD patterns for **2** at 293 K are similar to those simulated from X-ray single crystallographic data at 100 K (Fig. S6†).

The coordination environments of neutral and reduced from the crystal structures are significantly different (Fig. 2, 3, S1 and S4†). Since the ionic radius changes depending on the Ce valence state, the Ce–N_{iso} average distance is 2.432 Å for Ce$(obPc)_2$ and 2.418 Å for $Ce(Pc)_2$. On the other hand, it is 2.528 Å for **1** and 2.542 Å for **2** due to the changes in the ionic radii.[63,64] Considering the LF in the context of the oblate charge density distribution of the Ce^{3+} ion with $M_J = \pm 5/2$, both **1** and **2** exhibit uniaxial magnetic anisotropies with either SAP and/or SP geometries. Therefore, **1** and **2** should exhibit SMM characteristics.[24] However, referring to the *ab initio* calculations on single ion Ce^{3+} complexes by Singh *et al.*, zero-field SMM behaviour is unlikely to occur in the $D_{4d/4h}$ geometry of **1** and **2**.[29] Thus, based on the crystal structure data, we conducted a computational chemistry approach to investigate the presence of uniaxial anisotropy (details will be explained in the following section on magnetic measurements and theoretical calculations).

Electronic structure characterisations

In $Ce(Pc)_2$, the tetravalent Ce state can be changed to the trivalent state since the Ce^{3+} to Ce^{4+} oxidation midpoint potential is relatively low.[65–68] On the other hand, Ce–Pc triple-decker complexes in which Ce^{3+} ions are stable can be oxidised to the Ce^{4+} state.[47,69] Both oxidation states of these complexes are stable in solution, and the complexes in either oxidation state can be isolated as solids. Since $Ce^{4+/3+}$ ions of Ce multiple-decker complexes can undergo electrochemical and chemical oxidation–reduction, switchable metal centres [$4f^0$ (nonmagnetic) ⇌ $4f^1$ (paramagnetic)] are possible. Several examples of switching between SMMs and paramagnetic properties and spin dynamics phenomena by using the redox process of the metal ion and ligands have been reported.[7,67–83] Therefore, since Ce–Pc multiple-decker complexes can be reversibly switched from diamagnetic to paramagnetic/SMMs, they are attractive for use as switches.

In both CV and DPV, $Ce(obPc)_2$ showed five redox waves (Fig. S7-1 and S7-2, Tables S3-1 and S3-2†). $Ce(obPc)_2$ undergoes one more redox process than $Tb(obPc)_2$ does because the Ce ion is redox-active, unlike the Tb ion. The five redox waves observed for $Ce(obPc)_2$ have also been observed for other Ce double-decker complexes.[48,49] From the redox properties of Ce$(Pc)_2$, Red1 of the $Ce(obPc)_2$ was attributed to the Ce^{4+}/Ce^{3+} couple.[48,49,84]

Fig. S8-1† shows a UV-vis-NIR absorption spectrum of Ce$(obPc)_2$. Absorption bands were observed at 357, 476, 649, and 688 nm. The absorption at 357 nm is the Soret band, and the absorptions at 649 nm and 688 nm were attributed to the Q bands. In addition, the broad absorption band at 476 nm was assigned to a ligand-to-metal charge transfer (LMCT) transition from the Pc ligand to the Ce^{4+} ion.[47,69] On the other hand, when $Ce(obPc)_2$ was reduced with hydrazine monohydrate, the bands shifted slightly. The Soret band was at 354 nm, and the Q band was at 642 nm. The LMCT band (448 nm) observed for $Ce(obPc)_2$ was also observed for **1** due to the mixed valence of the $Ce^{4+/3+}$ ion with IET between the Ce^{3+} ion and the Pc ligand. On the other hand, the LMCT band was not observed for **2** due to the Ce^{3+} ion, indicating the effects of the Ce^{4+} ion in the complex (Fig. S8-2†). Considering the charge balance of the $[Ce(obPc)^2]^-$ unit, no radicals are generated in the reduced Pc ligands (Fig. S8-1†).[47] The anionic state of the Pc ligands was estimated to be $[Ce^{3+}(obPc^{2-})(obPc^{2-})]^-$ and $[Ce^{4+}(obPc^{2.5-})(obPc^{2.5-})]^-$, respectively. The absence of the intervalence(IV) absorption band in the near-infrared region above 1200 nm indicates that there are no π radicals on the Pc ligands (Fig. S8-1 and S8-2†). On the other hand, when $Ce(obPc)_2$ is oxidised by one electron, it becomes cationic, $[Ce^{4+}(obPc)^{\bullet-}(obPc)^{2-}]^+$, and an IV absorption band is observed in the near-infrared region (Fig. S8-3†).[47] In other words, spectroscopic measurements clearly show that no radicals are present on the Pc ligands of the $[Ce(obPc)^2]^-$ unit in **1**. From the spectrum, the reduced form $[Ce^{3+}(obPc)^{2-}(obPc)^{2-}]^-$ could be prepared using hydrazine monohydrate. $Ce(Pc)_2$ can also be reduced using the same method to synthesise $[Ce(Pc)_2]^-$. In other words, it is possible to synthesise **1** and **2** by chemical reduction (refer to the Experimental section).

It has been reported that the vibrational mode around 880 cm^{-1} in the IR spectrum is sensitive to the ionic radius of

lanthanoids.[63] For $Ce(Pc)_2$, it is 883 cm^{-1}, but the band is at 878 cm^{-1} for **2**. In addition, pyrrole stretching (1300–1350 cm^{-1}) and isoindole stretching (1370–1484 cm^{-1}) are sensitive to the ionic radius of lanthanoid ions, and we confirmed that they were shifted for $Ce(Pc)_2$ and **2** (Fig. S9-1 and S9-2†).[85] On the other hand, the peak near 880 cm^{-1} for the vibration mode of Ce $(obPc)_2$ and **1** was not shifted. However, the isoindole stretching frequencies were different, reflecting the oxidation state of the Ce ions (Fig. S9-3 and S9-4†).

For neutral $Ce(Pc)_2$, the IET of $[Ce^{4+}(Pc)^{2-}(Pc)^{2-}] \rightleftharpoons [Ce^{3+}(Pc)^{\bullet-}(Pc)^{2-}]$ occurs because the energy level of the Ce^{3+} ion $4f^1$ orbital is very close to the energy level of the $Pc^{\bullet-}$ frontier orbital (Fig. S10†).[48,63] Furthermore, for $Ce[(15C5)_4Pc]_2$ ($(15C5)_4Pc$ = bis-[tetra-(15-crown-5)-phthalocyaninato]) Langmuir monolayers, molecular orientation-induced IET has been observed.[86] Recently, findings indicate the mitigation of IET in $Ce(Pc)_2$ upon adsorption onto an Au(111) substrate, thereby enabling the discernment of the $[Ce^{3+}(Pc)^{\bullet-}(Pc)^{2-}]$ state. This observation implies that IET can be regulated through the manipulation of the interface.[53,87]

XAFS allows element-selective measurements, from which information on the local structure and electronic states can be obtained. XAFS spectra are analysed in the energy region from the absorption edge, divided into XANES (from the absorption edge to about 50 eV) and EXAFS (from the XANES region to about 1000 eV). In particular, XANES spectra provide information on the electronic and geometric structures of X-ray absorbing atoms. We measured XANES spectra to investigate the electronic states of several types of Ce-based compounds (Fig. 4). When analysing XANES spectra, the simplest evaluation method is the fingerprint method, which estimates the electronic state and geometric structure by measuring the $Ce(Pc)_2$ based complexes and evaluating the degree of spectral matching. Therefore, we compared the spectra with previously reported analogous compounds and estimated the valence state of the Ce ions.[48]

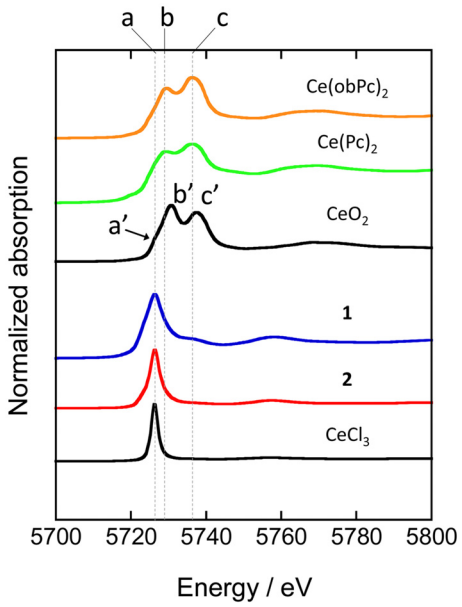

Fig. 4 Ce L_{III}-edge XANES spectra of reference materials (CeO_2 and $CeCl_3$) and $Ce(Pc)_2$ based complexes. See ESI for the assignment of each peak.

XANES spectra of neutral and reduced $Ce(Pc)_2$ derivatives were acquired to clarify the valence state of the Ce ion in **1**, the energy difference between 2p and 5d levels of the electronic states of Ce^{3+} and Ce^{4+} ions is different by *ca.* 10 eV.[88] Ce L_{III}-edge spectra of **1** and **2** are shown in Fig. 4, together with those of reference samples CeO_2 and $CeCl_3$. A white-line peak for the Ce^{3+} state appears at 5726 eV (labeled as a), which is associated with the 2p → $4f^15d$ dipole-allowed transition.[55,56,89] For **1** and **2**, a white-line peak appeared at 5726 eV at the same energy as the white line of $CeCl_3$. However, the feature in spectra of **1** and **2** was slightly broader than that of $CeCl_3$. In addition, the absorption labeled c (5736 eV, 2p → $4f^05d$ transition) in the spectrum of **1** is probably due to the influence of the electron-donating alkoxy substituents, as pointed out by Bian *et al.*[48] Peak c was not observed in the spectrum of unsubstituted **2**. On the other hand, the two absorption energies observed for $Ce(Pc)_2$ and $Ce(obPc)_2$ were at lower energies than that of CeO_2 (labeled a′, b′ and c′ in Fig. 4).[48] These absorbance energy shifts are due to differences in the coordination environments and electronic structures.

The mixed valence state of Ce ion has been reported to be the Ce double-decker complexes.[48,63,87] The characteristics of the valence state for the Ce double-decker complexes are shown in Tables S4-1 and S4-2.† Table S4-2† shows the results of estimating the ratio of Ce^{3+} and Ce^{4+} ions using a Gaussian function from XANES spectrum (Fig. S11†). From the analysis, **2** has 1 mol of Ce^{3+} ions, and **1** has *ca.* 0.8 mol of Ce^{3+} ions with *ca.* 0.2 mol of Ce^{4+} ions. The spectral shape, absorption energy, and relative intensity of XANES spectra reflect the electronic structures, which have the weight of orbital mixing between the Ce ion and the ligands. The IET indicates that the f orbital of **1** is mixed with the $obPc_2$ ligands. The valence state of the Ce ion in each compound is reflected in the magnetic properties (*vide infra*).

Static-field magnetic properties

From the dc measurements, $Ce(obPc)_2$ and $Ce(Pc)_2$ exhibited diamagnetic properties above 10 K. For $Ce(obPc)_2$, a diamagnetic response was generated at 1.8 K (Fig. S12†). On the other hand, the field dependence of the magnetisation (*M*–*H*) for powder samples of $Ce(Pc)_2$ exhibits paramagnetic properties at 2 K (Fig. S13†). Here, focusing on the IET, both $Ce(obPc)_2$ and $Ce(Pc)_2$ are in Ce^{4+}/Ce^{3+} mixed valence states, with the paramagnetic signature observed for $Ce(Pc)_2$ indicative of a higher ratio of Ce^{3+} in comparison to $Ce(obPc)_2$ (Fig. S10 and Table S4-2†).[63]

Fig. 5a and b show the magnetic susceptibilities (χ_M) of **1** and **2** in the temperature (T) range of 1.8–300 K in an H of 5 kOe. For clarity, we first show the results for **2**, which has 1 mol of Ce^{3+} ions (Fig. 5b). The value of $\chi_M T$ of **2** at room T was 0.68 cm^3 K mol^{-1}, which is lower than the value for one

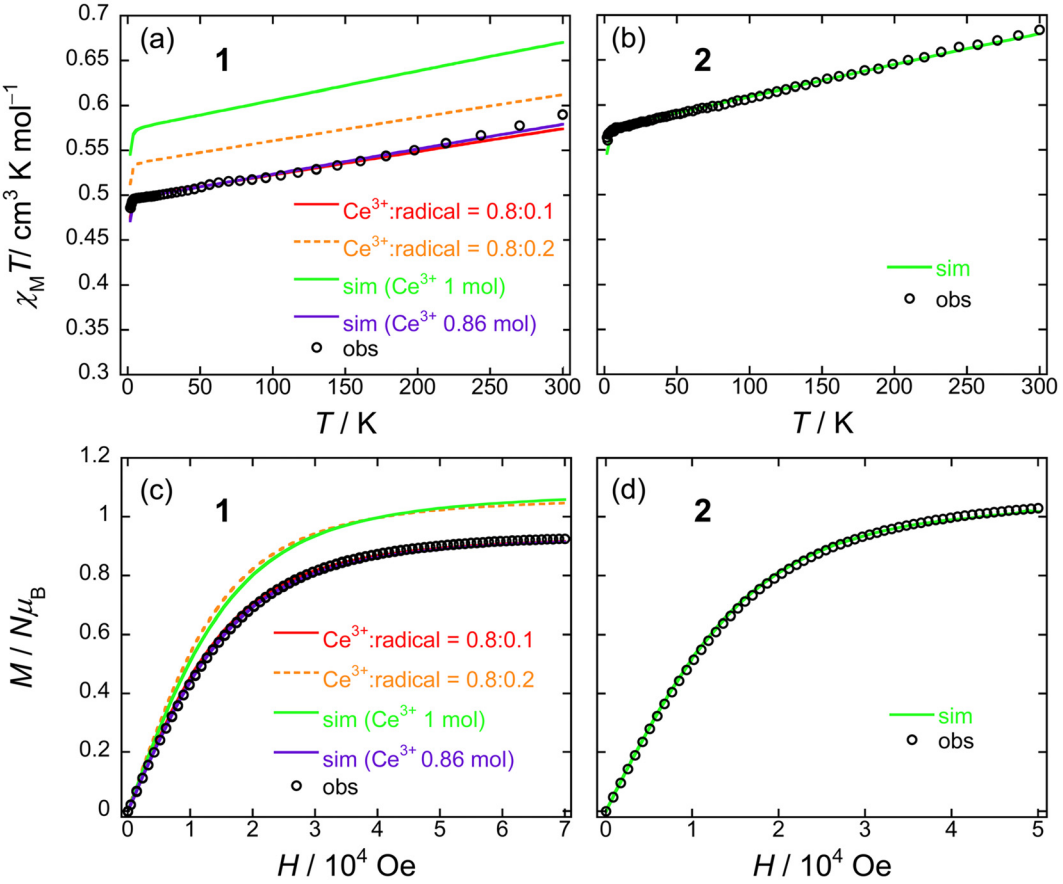

Fig. 5 T dependence of $\chi_M T$ for powder samples of (a) **1** and (b) **2** obtained in the T range of 1.8–300 K in an H of 5 kOe. Field dependence of the magnetisation (M–H) measured on powder samples of (c) **1** and (d) **2** at 1.8 K. The solid lines were simulated by using the PHI software package (see main text and Fig. S15†). The ligand field parameters (LFPs) of **1** and **2** were obtained by using CASSCF calculations (see main text).

free isolated Ce^{3+} ion (0.8 cm^3 K mol^{-1}, $^2F_{5/2}$, g_J = 6/7). The gradual decrease in $\chi_M T$ mainly originates from LF effects, such as the thermal depopulation of the Stark sublevels. This behaviour has been reported for other Ce^{3+} complexes.[25,35] The field dependence of the magnetisation (M–H) on powder samples of **2** was measured at 1.8 K (Fig. 5d and S14†). The theoretical saturated magnetisation (M_{sat}) value of completely oriented Ce^{3+} ions (1 mol) with uniaxial anisotropic and ground KDs of $M_J = \pm 5/2$ was $2.14N\mu_B$ [$M_{sat} = g_J\,(6/7) \times M_J\,(5/2)$]. However, M_{sat} for **2** was $1.03N\mu_B$ which is close to the expected M_{sat} of a randomly oriented Ce^{3+} ion (1 mol) with uniaxial anisotropy ($M_{sat} = 1/2g_JM_J = 1.07N\mu_B$). In addition, using a pseudo-spin $S^{eff} = 1/2$ approximation approach for M_{sat} of **2** at 1.8 K, M_{sat} (= $1/2g_Z^{eff}S^{eff}$) was determined to be $1N\mu_B$ using $g_Z^{eff} \approx 4$ from the CASSCF calculations (Table S5†). The T dependence of $\chi_M T$ and H dependence of M data for **2** were used to determine the magnetic properties using the PHI software package with the LFPs (Table S6†) from CASSCF calculations.[90] Experimental results could be explained using the parameters obtained from the theoretical calculations (*c.f.* Theoretical calculation section).

On the other hand, **1** exhibits a mixed valence state with Ce^{3+} (*ca.* 0.8 mol) and Ce^{4+} ions (*ca.* 0.2 mol) as determined by using XANES analysis (Table S4†). Therefore, the $\chi_M T$ value of **1** is smaller than that of **2** (1 mol of Ce^{3+} system) in the T range used (Fig. 5a). In addition, the M_{sat} value of **1** is smaller than that of **2** (Fig. 5c). The T dependence of $\chi_M T$ and H dependence of the M data for **1** were used to determine the magnetic properties by using the PHI software package with the LFPs (Table S6†) from CASSCF calculations (*c.f.* Theoretical calculation section).[90] First, when we performed a simulation on **1** with 1 mol of Ce^{3+} ion, it had similar behaviour to **2**, and the differences reflect the LFPs (Fig. 5a and c: green solid lines). The results of this simulation differ significantly in the theoretical values on the vertical axis compared to the experimental values. Therefore, we performed a simulation with the net abundance ratio of Ce^{3+} ion in **1** with 0.86 mol, and we were able to nearly reproduce the experimental values (Fig. 5a and c: violet solid lines). This is effective when assuming $Ce^{3+} : Ce^{4+} = 0.8 : 0.2$ based on XANES spectrum analysis (Table S4-2†) and attributing magnetic properties to the Ce^{3+} component. On the other hand, the orange dashed line represents the results of the simulation with $[Ce^{3+}(obPc)^{2-}(obPc)^{2-}]^- : [Ce^{4+}(obPc)^{2-}(obPc)^{\bullet 3-}]^- = Ce^{3+} : radical = 0.8 : 0.2$ based on XANES spectrum analysis (Table S4-2†). However, this did not reproduce the experimental data (Fig. 5a and c).

The experimental values were nearly reproduced by the red solid line (Ce^{3+} : radical = 0.8 : 0.1). The simulation results of the *M*–*H* curve are presented in Fig. S15.† A $\chi_M T$ value for the radical (S = 1/2) of 0.375 cm^3 K mol^{-1} was used in the simulation. In these simulations, the Ce^{3+} and radical components are added together. Considering the XANES spectrum and magnetic propeties of the neutral species (Table S4-2 and Fig. S13†) and the simulation results of the *M*–*H* curve (Fig. S15†), the magnetisation value of the radicals in the $[Ce^{4+}(obPc)^{2-}(obPc)^{\bullet 3-}]^-$ unit resulting from IET are lower than the ratio obtained from the XANES spectrum. However, it is currently unknown how stable the $[Ce^{4+}(obPc)^{2-}(obPc)^{\bullet 3-}]^-$ state, which results from IET, is.

Both **1** and **2** have uniaxial magnetic anisotropy, and the origin is the Ce^{3+} ion with ground KDs of $M_J = \pm 5/2$. The magnetic behaviour can be reproduced with the LFP obtained from CASSCF calculations. By considering the net abundance ratio of the Ce^{3+} ion from XANES spectral analysis (Table S4†), it is possible to understand the magnetic behaviour of **1**. In comparison to the Tb^{3+} system, the coordination environments of **1** and **2** are markedly different, but there are no drastic differences in their magnetic behaviours.[91] In other words, the presence of structural polymorphs of **1** is thought to have little effect on the T dependence of the $\chi_M T$ values and the *M*–*H* properties.

Dynamic magnetic properties

The ac magnetic susceptibilities of powder samples of **1** and **2** were acquired. The in-phase (χ'_M) and out-of-phase (χ''_M) signals were ν dependent in the range of 1–1000 Hz in different T ranges. No ν dependence was observed down to 2 K in an H of zero, indicating that **1** and **2** undergo slow magnetic relaxation phenomena in an $H \neq 0$ (Fig. S16†).

To investigate the magnetic relaxation properties of **1** and **2**, ν dependent measurements were performed in the ν range of 1–1000 Hz at 4 K (Fig. S17 for **1** and Fig. S18† for **2**). When an H was not applied, no ac signal was observed. This is the same behaviour as that reported for other Ce^{3+} complexes, indicating that QTM is dominant.[24–40] However, when an $H > 0$ Oe was applied, field-induced slow magnetic relaxation behaviour was observed for **1** and **2**. To determine the slow magnetic single relaxation processes of **1** and **2**, we analysed the data by using a generalised Debye model (eqn (S1)–(3)†) to estimate τ.[92] Fig. 6a shows the H dependence of τ. These results confirm that QTM is suppressed in an H and that a direct process is enhanced. Since QTM is suppressed when an H is applied, τ becomes slow with an increase in H and reaches a maximum (τ_{max}). The magnetic field ($H_{\tau_{max}}$) at which the τ values of **1** and **2** exhibit the lowest rate is 250 Oe for **1** and 750 Oe for **2**. In addition, the τ for **1** is approximately twice as slow as that of **2** (Fig. S19†). τ is almost constant between 100 and 3000 Oe due to the Raman process. Above 4000 Oe, $\tau \propto H^{-n}$ with $n = 4$ due to the Kramers Ce^{3+} ion, suggesting that the direct process is promoted (eqn (1)).

$$\tau^{-1} = a_1/(1 + a_2H^2) + bH^4T + c \quad (1)$$

where the first and second terms are from the tunnelling and direct processes, respectively, and the constant c represents the

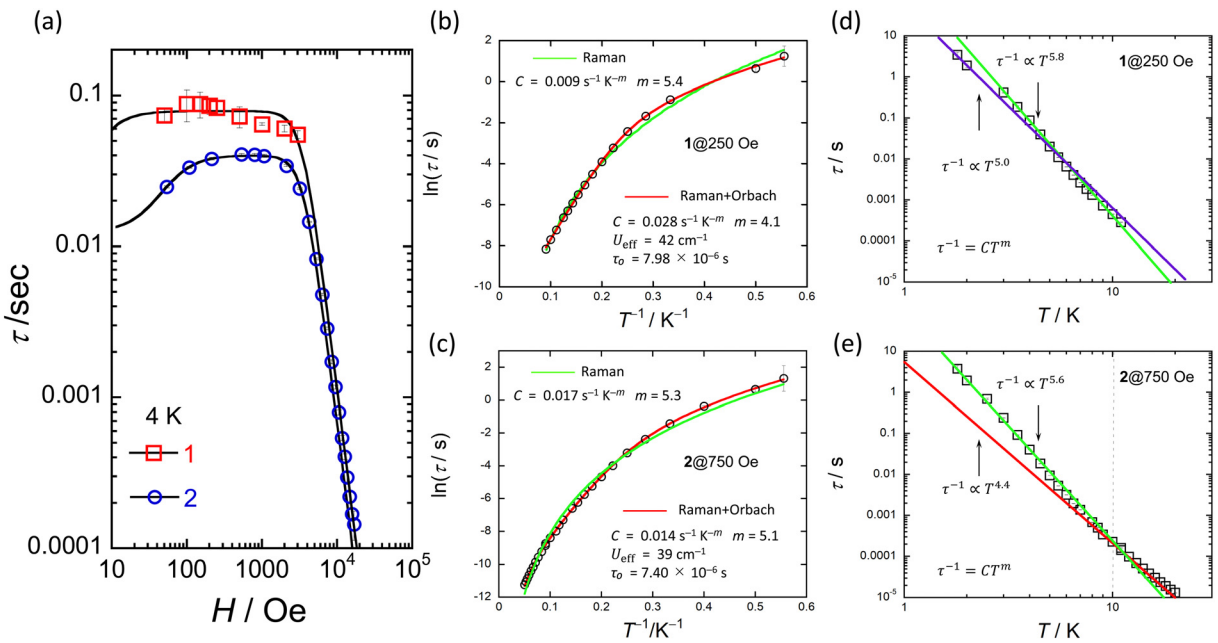

Fig. 6 (a) H dependence of τ for **1** and **2** at 4 K obtained from χ''_M *versus* ν plots (Fig. S17 and S18†). Black solid lines were fitted by using eqn (1). (b) and (c) shows the T dependence of τ of **1** and **2** in the appropriate H obtained from χ''_M *versus* ν plots (Fig. S20 and S21†). Red solid lines were fitted by using eqn (2). Green solid lines were fitted by using $\tau^{-1} = CT^m$. (d) and (e) shows the logarithmic representation of τ below 10 K of **1** and **2** in each appropriate H. Solid lines were fitted by using $\tau^{-1} = CT^m$. The best fits were obtained for the experimental data using the parameters described in the inset of figures (b–e), respectively.

field–independent terms, which are a Raman process (Table S7†).[33,35]

To investigate the slow magnetic relaxation phenomena in detail, we prepared χ'_M and χ''_M *versus* ν plots. We analysed the data by using a generalized Debye model (eqn (S1)–(S3)†) to estimate τ for **1** in an H of 250 Oe and **2** in an H of 750 Oe (Fig. S20 for **1** and S21† for **2**). For **1**, a T range of 1.8–11 K and a ν range of 1–1000 Hz were used, and for **2**, a T range of 1.8–20 K and a ν range of 1–10 000 Hz were used (Fig. S21 and S22†). Fig. 6b and c show the T dependences of τ of **1** and **2** (Fig. S23†). The U_{eff} values of **1** and **2** were estimated from an Arrhenius plot (τ *versus* T^{-1}) to be 42 cm^{-1} (60 K) and 40 cm^{-1} (58 K) with τ_0 values of 7.98×10^{-6} s and 7.40×10^{-6} s, respectively. C was determined to be 2.8×10^{-2} s^{-1} K^{-m} (m = 4.1) for **1** and 1.4×10^{-2} s^{-1} K^{-m} (m = 5.1) for **2** from Arrhenius plots using eqn (2), where the first and second terms denote Raman and Orbach processes.[93]

$$\tau^{-1} = CT^m + \tau_0^{-1}\exp(-U_{eff}/k_BT) \quad (2)$$

The U_{eff} (≈40 cm^{-1}) and τ_0 (≈10^{-6} s) values of **1** and **2** are larger than those of related Ce^{3+} SMMs.[24–30,33–40] Therefore, we must consider another magnetic relaxation process instead of an Orbach process due to the small number of phonons below 10 K. The energy gap between the ground state and the first excited state estimated from CASSCF calculations, which will be explained later, was approximately 900 cm^{-1}, which is one order of magnitude larger than the U_{eff} estimated from the T dependence of τ. From the results of the CASSFC calculations, it is necessary to consider under-barrier Raman processes.[35,42,43] It is possible to reproduce the T dependence of τ considering the Raman process ($\tau \propto T^m$; m = 5.4 for **1** and 5.3 for **2**) (Fig. 6b and c). In addition, we found a linear relationship from the logarithmic representation of τ *versus* T plot for **1**, which suggests that the magnetic relaxation mechanism may be a Raman process (Fig. 6d and e).[93] A linear relationship at T < 10 K can be reproduced when m = 5.0–5.8. It has been reported that m can take values from 1 to 6 for Raman processes involving optical-acoustic phonons.[94] In addition, the vibrational energy barriers (U_R) of **1** and **2** were estimated to be *ca.* 40 cm^{-1}.[19–22] Thus, we are considering measuring the vibrational modes in the terahertz region. The Raman process of Ce^{3+}-based single-ion SMM is summarised in Table 1.[30,95]

From the T and H dependences of τ, **1** and **2** exhibit field-induced SMM characteristics. As reported by Singh *et al.*, it is clear that **1** and **2** do not exhibit magnetic relaxation characteristics without an H.[29] In addition, the magnetic relaxation phenomenon of **1** is accompanied by IET with spin-phonon coupling because the ionic radius of the Ce ion changes between 1.14 Å (trivalent) and 0.96 Å (tetravalent). The ionic radius of the Ce ion in $Ce(Pc)_2$ is 1.01 Å, which is intermediate between those for Ce^{3+} and Ce^{4+} ions in the 8-coordinate system.[63,64] Since the ionic radius obtained from X-ray structure analysis is an averaged value, we performed XAFS, which is effective for separating and observing local structures and electronic states in an element selective manner. In addition, the timescale of IET is slower than the measurement time of XAFS (≈10^{-17} s). From spectroscopic measurements, the holes generated within the Ce double-decker complex are delocalized across the two ligand systems on both vibrational (10^{-13} s) and electronic (10^{-15} s) timescales.[96] In other words, this timescale is related to the electron transfer rate between the Ce ion and the Pc ligands. In addition, the timescale of valence fluctuations for $Ce^{4+/3+}$ ions, which is on the order of 10^{-13} s, changes with the molecular vibration (phonon frequency (ω)).[97] The dynamic disorder with ω in SMMs mainly depends on the intramolecular vibrations. Therefore, we should consider the influence of IET with dynamic disorder and phonon coupling on the magnetic relaxation phenomena in addition to spin-phonon interactions (Fig. 7).[98] In this case, since the τ of **1** is nearly twice as slow as that of **2**, the influence of IET cannot be ignored.

On the other hand, since the Ce···Ce distance between molecules is more than 10 Å, we believe that Ce···Ce interactions do not influence the magnetic properties of **1** and **2**. Therefore, magnetically diluted samples with non-magnetic isostructural complexes were not tested. For Tb^{3+} and Dy^{3+}

Table 1 Optimised parameters from Raman process of single ion Ce^{3+} based single-molecule magnets

Complexes	Coordination number and/or pseudo-symmetry	H/Oe	C/s^{-1} K^{-m}	m/s^{-1}	Direct	Ref.
TBA[Ce(obPc)] (**1**)	8-Coordinate sandwich saddle-shaped distorted D_{4h} or D_{4d}	250	0.009	5.4	—	This work
TBA[Ce(Pc)] (**2**)	8-Coordinate sandwich D_{4h}	750	0.017	5.3	—	This work
$[CeCd_3(Hquinha)_3(n\text{-}Bu_3PO)_2I_3]\cdot 3EtOH\cdot 2H_2O$	8-Coordinate hexagonal bipyramidal D_{6h}	1500	—	6.9	—	35
[Ce(fdh)$_3$(bpy)] (fdh = 1,1,1-fluoro-5,5-dimethyl-hexa-2,4-dione)	8-Coordinate paddle-wheel shape	2000	0.4	6	—	39
$[Ce(NO_3)_3L]$ (L = ^{t}BuPO(NHiPr)$_2$)	9-Coordinate muffin-like structure	200	1.44	6.8	99.5	40
$[Ce_{0.29}La_{0.71}(NO_3)_3L_3]$		30	0.8	7.55	306.5	40
[Ce(18-crown-6) (Cl_4Cat) (NO_3)] (X_4Cat = tetrahalocatecholate)	10-Coordinate sphenocorona D_{6h}	1500	1.22	5 (fixed)	—	42
[Ce(18-crown-6) (Br_4Cat) (NO_3)]	10-Coordinate sphenocorona D_{6h}	800	1.87	5 (fixed)	—	42
$[Ce(Cp^{ttt})_2\{(C_6F_5\text{-}\kappa^1\text{-}F)B(C_6F_5)_3\}]$ (Cp^{ttt} = $C_5H_2{}^tBu_3$-1,2,4)	Bent-metallocene structure	1000	0.0308	5.4	—	43
$[Ce(Cp^{ttt})_2(Cl)]$	Bent-metallocene structure	1000	0.00475	6.5	—	43

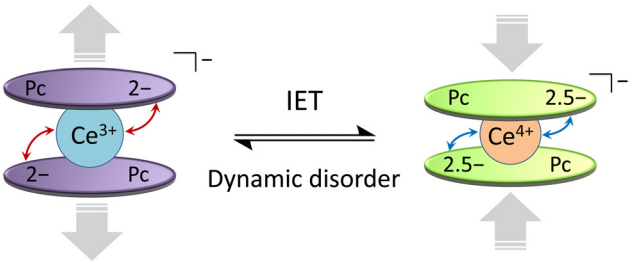

Fig. 7 Schematic illustration of the intramolecular electron transfer (IET) in $[Ce(obPc)_2]^-$ unit of **1** with the dynamic disorder (see main text).

complexes, magnetic dilution is possible with the isostructural Y^{3+} complex. However, since the structures of **1**, **2**, and the Y^{3+} complex are significantly different due to the different ionic radii, magnetic dilution is impossible.[64] On the other hand, La^{3+} ions ($4f^0$: 1.16 Å) have approximately the same ionic radius of Ce^{3+} ions ($4f^1$: 1.14 Å) and is nonmagnetic, meaning isostructural $TBA^+[La(obPc)_2]^-$ and $TBA^+[La(Pc)_2]^-$ complexes should form. Thus, it should be possible to dilute **1** and **2** magnetically.[40] In addition, although structural polymorphism is thought to have little effect on the SMM properties of **1** and **2**, we plan to investigate this point in detail with $Ce(Pc)_2$-based complexes in several coordinating environments.

The origin of the uniaxial magnetic anisotropy of **1** and **2** and the magnetic relaxation phenomenon will be discussed in the next section *via ab initio* calculations (*vide infra*).

Theoretical studies on the magnetic anisotropy and spin dynamics mechanism

To gain insight into the magnetic structures of $[Ce(obPc)_2]^-$ for **1** and $[Ce(Pc)_2]^-$ for **2**, CASSCF calculations were performed using the crystal structure coordinates without TBA^+. The ground doublet of $[Ce(obPc)_2]^-$ and $[Ce(Pc)_2]^-$ was composed of 99.2% and 98.5% of $M_J = \pm 5/2$, respectively, confirming the axial magnetic anisotropy (Table S5†). The magnetic easy axis of $[Ce(obPc)_2]^-$ and $[Ce(Pc)_2]^-$ coincides with the quasi-C_4 axis, which is consistent with the oblate electron density of the Ce^{3+} ion stabilised by the axial ligand fields of the Pc^{2-} ligands (Fig. S24†). However, the small difference in the composition of $M_J = \pm 5/2$ of the ground doublet results in the difference in the g_z values of the ground doublet (4.01 for $[Ce(obPc)_2]^-$ and 3.96 for $[Ce(Pc)_2]^-$). The magnitude of the LF splitting for $[Ce(obPc)_2]^-$ is greater than that for $[Ce(Pc)_2]^-$ due to the larger axial component of the LFPs (B_{20} and B_{40}) for $[Ce(obPc)_2]^-$ (Table S6†). The first excited KDs of $[Ce(obPc)_2]^-$ and $[Ce(Pc)_2]^-$ were located at 955 and 921 cm^{-1}, respectively (Fig. S25-1, S25-2, and Table S7†). These energy values are much larger than the U_{eff} values expected from the experimental ac magnetic measurements (Fig. 6b and c). In other words, the magnetic relaxations *via* an excited LF level (Orbach process and thermally assisted QTM) do not occur in the relaxation mechanism (see dynamic magnetic properties). The magnetic dipolar transition moment of the ground doublet of $[Ce(obPc)_2]^-$ (0.151) is smaller than that of $[Ce(Pc)_2]^-$ (0.202) due to the better axiality of $[Ce(obPc)_2]^-$ as shown by the larger g_z value (Table S5-3†). In other words, the magnetic relaxations driven by a transversal component of the internal magnetic field (QTM) are suppressed for $[Ce(obPc)_2]^-$ and not for $[Ce(Pc)_2]^-$, consistent with the slower τ and small $H_{\tau_{max}}$ values of **1** compared to **2**.[30] From theoretical investigations on Ce^{3+}-based SMMs reported by Singh *et al.*, $D_{4d/4h}$ geometries are unfavourable for axial magnetic anisotropy.[29] However, Ce^{3+}–Pc double-decker complexes shown here have strong axial magnetic anisotropy, although their point group symmetries are classified as $D_{4d/4h}$. There is no contradiction between our results and previous theoretical investigations because the axial magnetic anisotropy is due to the position of the negative charges on the axis rather than the point group symmetry. In the Ce^{3+}–Pc double-decker complexes, the coordinating N atoms gather in the axial position of the Ce^{3+} ion due to the small cavity of the Pc^{2-} ligands compared with the Ce^{3+} ion, enhancing the axial ligand field.

Conclusions and perspectives

In this study, we clarified the influence of IET on spin-phonon coupling for magnetic relaxation behaviour.[99] We focused on the fact that orbital mixing between Ce ions and π-conjugated planar ligands causes the IET and selected Ce–Pc-based double-decker compounds for this work.

We investigated the chemical conversion of the diamagnetic Ce^{4+} forms ($4f^0$) $Ce(obPc)_2$ and $Ce(Pc)_2$ into the paramagnetic Ce^{3+} forms ($4f^1$) **1** and **2**, both of which exhibit field-induced SMM behaviour. In particular, the Ce ion in **1** undergoes the mixed valence states of Ce^{4+}/Ce^{3+} *via* IET between the Ce ion and the Pc ligands. On the other hand, the valence state of the Ce ion in **2** is trivalent without IET. The valence states of the Ce ion in each compound are reflected in the magnetic properties. Since the magnetic relaxation time (τ) of **1** is nearly twice as slow as that of **2**, the dynamic disorder is expected due to the mixed valence states of Ce^{4+}/Ce^{3+}. From the magnetic field dependence of the spin dynamics, the appropriate magnetic field of **1** with IET is 250 Oe, which is smaller than that of **2** (750 Oe) without IET. If the magnetic field can be reduced by controlling the IET, it should be possible to prepare Ce-based SMMs without an external magnetic field.

The Ce^{4+}/Ce^{3+} mixed valence states due to IET can be controlled by changing the type of electron-donating groups and controlling the orbital mixing between the Ce ion and the ligands. In other words, it would be possible to control the valence state of the Ce ions by separating the frontier orbitals of the Pc ligands from the $4f^1$ orbital of the Ce^{3+} ion.[48] The above concepts apply not only to the mononuclear Ce–Pc double-decker complexes but also to dinuclear Ce–Pc multiple-decker complexes.[47,69] For example, an advantage of dinuclear Ce complexes is that the valence state of each Ce ion can be changed separately by changing the number of porphyrinoids ligands inserted between the Ce ions.[99] In addition, we have synthesised Ce–Pc multiple-decker complexes with up to seven layers of Pc ligands with four Cd^{2+} ions in between the Ce ions (quadruple- to septuple-decker complexes).[100,101] The modu-

lation of the spin dynamics *via* supramolecular chemistry holds promise for realizing Ce SMMs. Furthermore, proton switching,[102] dimerization,[103–105] fullerene co-crystals,[106] and one-dimensional expansion approaches[10,107] by regulating the coordination geometries and intermolecular interactions are conceivable.[108] The spin dynamics of a Ce ion can be altered by adjusting the interactions between conduction electrons (holes) due to molecular orbital overlap[53] and the interactions between frontier orbitals and Ce f orbitals induced by the distortions of the π-conjugated porphyrinoids with electron-donating substituents.

In addition, we will use these Ce complexes to investigate the control of the spin dynamics due to IET. The $Ce(Pc)_2$ system exhibits a distinctive feature wherein IET occurs between the Ce ion and Pc ligands, thus manifesting its intricate electronic configuration. In contrast, mixed valence states have been documented for numerous metal complexes and inorganic compounds. To the best of our knowledge, instances of IET occurring between other Ln ions and Pc ligands have not been reported. However, the electron transfer between Ln ions and radical ligands significantly influences the magnetic properties.[109–112] In other words, diverse valence states owing to electron transfer between Ln ions and ligands are possible. Thus, Ln ion-based SMMs exhibiting mixed valence states can be synthesised through judicious molecular design. Furthermore, this paper was centred on the investigation of the IET phenomenon in its reduced form $[Ce(obPc)_2]^-$. However, from the analysis of the electronic spectra, in solution, cationic $[Ce(obPc)_2]^+$ forms through the one-electron oxidation of **1**, whereas a radical species concurrently forms on the Pc ligands. Our ongoing research endeavours will further explore the intricacies of electron transfer dynamics between Ce^{4+} and $Pc^{\bullet-}$ ligands, extending our inquiry into solid state environments. By applying IET to the spin dynamics of Ce porphyrinoid-based complexes, it will be possible to investigate the effects of dynamic disorder on SMM properties.

Author contributions

K. K. designed the study and the main conceptual ideas and supervised the project. K. K., M. S., T. S. Y. H., T. Y., and K. K. collected and analysed the data. All authors aided in interpreting the results and prepared the manuscript. All authors discussed the results and commented on the manuscript.

Conflicts of interest

There are no conflicts to declare.

Acknowledgements

This work was partially supported by a Grant-in-Aid for Scientific Research (C) (grant no. 21K05010, no. 15K05467), Grant-in-Aid for Young Scientists (B) (grant no. 24750119), Grant-in-Aid for Scientific Research (S) (grant no. 20225003) from JSPS KAKENHI, CREST (JPMJCR12L3) from JST. The X-ray absorption fine structure was collected on the BL9A beamline in the Photon Factory of the High Energy Accelerator Research Organization (KEK, proposal no. 2017P016, 2019G117). Y. H. acknowledges Prof. Takashi Kajiwara (Nara Women's University) for computational resources and PXRD measurements.

References

1 L. Bogani and W. Wernsdorfer, *Nat. Mater.*, 2008, **7**, 179–186.
2 M. N. Leuenberger and D. Loss, *Nature*, 2001, **410**, 789–793.
3 J. Tejada, E. M. Chudnovsky, E. del Barco, J. M. Hernandez and T. P. Spiller, *Nanotechnology*, 2001, **12**, 181–186.
4 D. Gatteschi, R. Sessoli and J. Villain, *Molecular Nanomagnets*, Oxford University Press, 2006.
5 C. J. Wedge, G. A. Timco, E. T. Spielberg, R. E. George, F. Tuna, S. Rigby, E. J. L. Mcinnes, R. E. P. Winpenny, S. J. Blundell and A. Ardavan, *Phys. Rev. Lett.*, 2012, **108**, 107204-1–107204-5.
6 G. Aromí, D. Aguilà, P. Gamez, F. Luis and O. Roubeau, *Chem. Soc. Rev.*, 2012, **41**, 537–546.
7 W. Wernsdorfer, N. Aliaga-Alcalde, D. N. Hendrickson and G. Christou, *Nature*, 2002, **416**, 406–409.
8 J. D. Rinehart, M. Fang, W. J. Evans and J. R. Long, *Nat. Chem.*, 2011, **3**, 538–542.
9 F. S. Guo, B. M. Day, Y. C. Chen, M. L. Tong, A. Mansikkamäki and R. A. Layfield, *Angew. Chem., Int. Ed.*, 2017, **56**, 11445–11449.
10 K. Katoh, S. Yamashita, N. Yasuda, Y. Kitagawa, B. K. Breedlove, Y. Nakazawa and M. Yamashita, *Angew. Chem., Int. Ed.*, 2018, **57**, 9262–9267.
11 D. N. Woodruff, R. E. P. Winpenny and R. A. Layfield, *Chem. Rev.*, 2013, **113**, 5110–5148.
12 F. Habib and M. Murugesu, *Chem. Soc. Rev.*, 2013, **42**, 3278–3288.
13 H. L. C. Feltham and S. Brooker, *Coord. Chem. Rev.*, 2014, **276**, 1–33.
14 S. T. Liddle and J. Van Slageren, *Chem. Soc. Rev.*, 2015, **44**, 6655–6669.
15 P. Zhang, Y. N. Guo and J. Tang, *Coord. Chem. Rev.*, 2013, **257**, 1728–1763.
16 J. L. Liu, Y. C. Chen and M. L. Tong, *Chem. Soc. Rev.*, 2018, **47**, 2431–2453.
17 J. D. Rinehart and J. R. Long, *Chem. Sci.*, 2011, **2**, 2078–2085.
18 C. A. Gould, K. R. McClain, D. Reta, J. G. C. Kragskow, D. A. Marchiori, E. Lachman, E. S. Choi, J. G. Analytis, R. D. Britt, N. F. Chilton, B. G. Harvey and J. R. Long, *Science*, 2022, **375**, 198–202.

19 A. Lunghi, F. Totti, R. Sessoli and S. Sanvito, *Nat. Commun.*, 2017, **8**, 14620.
20 L. Gu and R. Wu, *Phys. Rev. Lett.*, 2020, **125**, 117203-1–117203-6.
21 Y. Ma, Y. Zhai, Q. Luo, Y. Ding and Y. Zheng, *Angew. Chemie Int. Ed.*, 2022, **61**, e202206022.
22 L. Scherthan, R. F. Pfleger, H. Auerbach, T. Hochdörffer, J. A. Wolny, W. Bi, J. Zhao, M. Y. Hu, E. E. Alp, C. E. Anson, R. Diller, A. K. Powell and V. Schünemann, *Angew. Chem., Int. Ed.*, 2020, **59**, 8818–8822.
23 K. R. Meihaus and J. R. Long, *J. Am. Chem. Soc.*, 2013, **135**, 17952–17957.
24 S. Hino, M. Maeda, K. Yamashita, Y. Kataoka, M. Nakano, T. Yamamura, H. Nojiri, M. Kofu, O. Yamamuro and T. Kajiwara, *Dalton Trans.*, 2013, **42**, 2683–2686.
25 J. J. Le Roy, I. Korobkov, J. E. Kim, E. J. Schelter and M. Murugesu, *Dalton Trans.*, 2014, **43**, 2737–2740.
26 S. Hino, M. Maeda, Y. Kataoka, M. Nakano, T. Yamamura and T. Kajiwara, *Chem. Lett.*, 2013, **42**, 1276–1278.
27 C. Takehara, P. L. Then, Y. Kataoka, M. Nakano, T. Yamamura and T. Kajiwara, *Dalton Trans.*, 2015, **44**, 18276–18283.
28 T. Shi, Y. Xu, M.-X. Li, C.-M. Liu, E. N. Nfor and Z.-X. Wang, *Polyhedron*, 2020, **188**, 114695.
29 S. K. Singh, T. Gupta, L. Ungur and G. Rajaraman, *Chem. – Eur. J.*, 2015, **21**, 13812–13819.
30 F. A. Mautner, F. Bierbaumer, R. C. Fischer, À. Tubau, S. Speed, E. Ruiz, S. S. Massoud, R. Vicente and S. Gómez-Coca, *Inorg. Chem.*, 2022, **61**, 11124–11136.
31 E. Regincós Martí, A. B. Canaj, T. Sharma, A. Celmina, C. Wilson, G. Rajaraman and M. Murrie, *Inorg. Chem.*, 2022, **61**, 9906–9917.
32 J. Mayans, L. Tesi, M. Briganti, M. E. Boulon, M. Font-Bardia, A. Escuer and L. Sorace, *Inorg. Chem.*, 2021, **60**, 8692–8703.
33 C. Takehara, P. L. Then, Y. Kataoka, M. Nakano, T. Yamamura and T. Kajiwara, *Dalton Trans.*, 2015, **44**, 18276–18283.
34 A. Ben Khélifa, M. S. Belkhiria, G. Huang, S. Freslon, O. Guillou and K. Bernot, *Dalton Trans.*, 2015, **44**, 16458–16464.
35 Q.-W. Li, R.-C. Wan, Y.-C. Chen, J.-L. Liu, L.-F. Wang, J.-H. Jia, N. F. Chilton and M.-L. Tong, *Chem. Commun.*, 2016, **52**, 13365–13368.
36 H. Wada, S. Ooka, T. Yamamura and T. Kajiwara, *Inorg. Chem.*, 2017, **56**, 147–155.
37 C. P. Burns, X. Yang, S. Sung, J. D. Wofford, N. S. Bhuvanesh, M. B. Hall and M. Nippe, *Chem. Commun.*, 2018, **54**, 10893–10896.
38 A. Upadhyay, K. R. Vignesh, C. Das, S. K. Singh, G. Rajaraman and M. Shanmugam, *Inorg. Chem.*, 2017, **56**, 14260–14276.
39 M. X. Xu, Y. S. Meng, J. Xiong, B. W. Wang, S. Da Jiang and S. Gao, *Dalton Trans.*, 2018, **47**, 1966–1971.
40 S. K. Gupta, S. Shanmugan, T. Rajeshkumar, A. Borah, M. Damjanović, M. Schulze, W. Wernsdorfer, G. Rajaraman and R. Murugavel, *Dalton Trans.*, 2019, **48**, 15928–15935.
41 N. Ishikawa, M. Sugita, T. Ishikawa, S. Y. Koshihara and Y. Kaizu, *J. Am. Chem. Soc.*, 2003, **125**, 8694–8695.
42 E. Rousset, M. Piccardo, M. E. Boulon, R. W. Gable, A. Soncini, L. Sorace and C. Boskovic, *Chem. – Eur. J.*, 2018, **24**, 14768–14785.
43 J. Liu, D. Reta, J. A. Cleghorn, Y. X. Yeoh, F. Ortu, C. A. P. Goodwin, N. F. Chilton and D. P. Mills, *Chem. – Eur. J.*, 2019, **25**, 7749–7758.
44 E. Moreno-Pineda, M. Damjanović, O. Fuhr, W. Wernsdorfer and M. Ruben, *Angew. Chem., Int. Ed.*, 2017, **56**, 9915–9919.
45 A. L. Wysocki and K. Park, *J. Phys.: Condens. Matter*, 2020, **32**, 274002.
46 N. M. Edelstein, P. G. Allen, J. J. Bucher, D. K. Shuh, C. D. Sofield, N. Kaltsoyannis, G. H. Maunder, M. R. Russo and A. Sella, *J. Am. Chem. Soc.*, 1996, **118**, 13115–13116.
47 T. H. Tran-Thi, T. A. Mattioli, D. Chabach, A. D. Cian and R. Weiss, *J. Phys. Chem.*, 1994, **98**, 8279–8288.
48 Y. Bian, J. Jiang, Y. Tao, M. T. M. Choi, R. Li, A. C. H. Ng, P. Zhu, N. Pan, X. Sun, D. P. Arnold, Z. Y. Zhou, H. W. Li, T. C. W. Mak and D. K. P. Ng, *J. Am. Chem. Soc.*, 2003, **125**, 12257–12267.
49 H. Isago, *J. Porphyrins Phthalocyanines*, 2014, **18**, 762–770.
50 M. D. Walter, C. H. Booth, W. W. Lukens and R. A. Andersen, *Organometallics*, 2009, **28**, 698–707.
51 K. Takahashi, M. Itoh, Y. Tomita, K. Nojima, K. Kasuga and K. Isa, *Chem. Lett.*, 1993, **22**, 1915–1918.
52 H. Hückstädt, A. Tutaß, M. Göldner, U. Cornelissen and H. Homborg, *Z. Anorg. Allg. Chem.*, 2001, **627**, 485–497.
53 I. Saiful, M. I. Hossain, K. Katoh, M. Yamashita, R. Arafune, S. M. Fakruddin Shahed and T. Komeda, *J. Phys. Chem. C*, 2022, **126**, 17152–17163.
54 B. Ravel and M. Newville, *J. Synchrotron Radiat.*, 2005, **12**, 537–541.
55 A. Bianconi, A. Marcelli, H. Dexpert, R. Karnatak, A. Kotani, T. Jo and J. Petiau, *Phys. Rev. B: Condens. Matter Mater. Phys.*, 1987, **35**, 806–812.
56 J. El Fallah, S. Boujana, H. Dexpert, A. Kiennemann, J. Majerus, O. Touret, F. Villain and F. Le Normand, *J. Phys. Chem.*, 1994, **98**, 5522–5533.
57 F. Neese, *Wiley Interdiscip. Rev. Comput. Mol. Sci.*, 2012, **2**, 73–78.
58 D. Aravena, F. Neese and D. A. Pantazis, *J. Chem. Theory Comput.*, 2016, **12**, 1148–1156.
59 F. Weigend and R. Ahlrichs, *Phys. Chem. Chem. Phys.*, 2005, **7**, 3297–3305.
60 S. H. Vosko, L. Wilk and M. Nusair, *Can. J. Phys.*, 1980, **58**, 1200–1211.
61 A. D. Becke, *J. Chem. Phys.*, 1993, **98**, 5648–5652.
62 P. J. Stephen, F. J. Devlin, C. F. Chabalowski and M. J. Frisch, *J. Phys. Chem.*, 1994, **98**, 11623–11627.
63 H. Isago and M. Shimoda, *Chem. Lett.*, 1992, 147–150.
64 R. D. Shannon, *Acta Crystallogr., Sect. A: Found. Crystallogr.*, 1976, **A32**, 751–767.

65 G. Ostendorp, H. W. Rotter and H. Homborg, *Z. fur Naturforsch. – B J. Chem. Sci.*, 1996, **51**, 567–573.
66 J. W. Buchler and M. Nawra, *Inorg. Chem.*, 1994, **33**, 2830–2837.
67 J. K. Duchowski and D. F. Bocian, *J. Am. Chem. Soc.*, 1990, **112**, 8807–8811.
68 M. Safarpour Haghighi, C. L. Teske and H. Homborg, *Z. Anorg. Allg. Chem.*, 1992, **608**, 373–380.
69 J. W. Buchler, M. Kihn-Botulinski, A. de Cian, J. Fischer, R. Weiss and H. Paulus, *J. Am. Chem. Soc.*, 1986, **108**, 3652–3659.
70 S. Fortier, J. J. Le Roy, C.-H. Chen, V. Vieru, M. Murugesu, L. F. Chibotaru, D. J. Mindiola and K. G. Caulton, *J. Am. Chem. Soc.*, 2013, **135**, 14670–14678.
71 A. I. Gaudette, I.-R. Jeon, J. S. Anderson, F. Grandjean, G. J. Long and T. D. Harris, *J. Am. Chem. Soc.*, 2015, **137**, 12617–12626.
72 J. Tong, S. Demeshko, M. John, S. Dechert and F. Meyer, *Inorg. Chem.*, 2016, **55**, 4362–4372.
73 B. S. Dolinar, S. Gómez-Coca, D. I. Alexandropoulos and K. R. Dunbar, *Chem. Commun.*, 2017, **53**, 2283–2286.
74 X. Zhu, S. Su, W. Cao, Y. Wen, S. Hu, X. Wu and T. Sheng, *Dalton Trans.*, 2017, **46**, 7267–7272.
75 G. N. Newton, S. Yamashita, K. Hasumi, J. Matsuno, N. Yoshida, M. Nihei, T. Shiga, M. Nakano, H. Nojiri, W. Wernsdorfer and H. Oshio, *Angew. Chem., Int. Ed.*, 2011, **50**, 5716–5720.
76 N. Ishikawa, M. Sugita, N. Tanaka, T. Ishikawa, S. Y. Koshihara and Y. Kaizu, *Inorg. Chem.*, 2004, **43**, 5498–5500.
77 M. Gonidec, E. S. Davies, J. Mcmaster and D. B. Amabilino, *J. Am. Chem. Soc.*, 2010, 1756–1757.
78 J. D. Rinehart, M. Fang, W. J. Evans and J. R. Long, *J. Am. Chem. Soc.*, 2011, **133**, 14236–14239.
79 D. E. Freedman, D. M. Jenkins, A. T. Iavarone and J. R. Long, *J. Am. Chem. Soc.*, 2008, **130**, 2884–2885.
80 L. Norel, M. Feng, K. Bernot, T. Roisnel, T. Guizouarn, K. Costuas and S. Rigaut, *Inorg. Chem.*, 2014, **53**, 2361–2363.
81 C. M. Dickie, A. L. Laughlin, J. D. Wofford, N. S. Bhuvanesh and M. Nippe, *Chem. Sci.*, 2017, **8**, 8039–8049.
82 A. Nava, L. Rigamonti, E. Zangrando, R. Sessoli, W. Wernsdorfer and A. Cornia, *Angew. Chem., Int. Ed.*, 2015, **54**, 8777–8782.
83 I.-R. Jeon, J. G. Park, D. J. Xiao and T. D. Harris, *J. Am. Chem. Soc.*, 2013, **135**, 16845–16848.
84 E. N. Tarakanova, O. A. Levitskiy, T. V. Magdesieva, P. A. Tarakanov, V. E. Pushkarev and L. G. Tomilova, *New J. Chem.*, 2015, **39**, 5797–5804.
85 F. Lu, M. Bao, C. Ma, X. Zhang, D. P. Arnold and J. Jiang, *Spectrochim. Acta, Part A*, 2003, **59**, 3273–3286.
86 S. L. Selektor, A. V. Shokurov, V. V. Arslanov, Y. G. Gorbunova, K. P. Birin, O. A. Raitman, F. Morote, T. Cohen-Bouhacina, C. Grauby-Heywang and A. Y. Tsivadze, *J. Phys. Chem. C*, 2014, **118**, 4250–4258.
87 J. Granet, M. Sicot, B. Kierren, S. Lamare, F. Chérioux, F. Baudelet, Y. Fagot-Revurat, L. Moreau and D. Malterre, *Nanoscale*, 2018, **10**, 9123–9132.
88 J. F. Herbst and J. W. Wilkins, *Phys. Rev. B: Condens. Matter Mater. Phys.*, 1982, **26**, 1689–1701.
89 W. Li, S. Yamada, T. Hashimoto, T. Okumura, R. Hayakawa, K. Nitta, O. Sekizawa, H. Suga, T. Uruga, Y. Ichinohe, T. Sato, Y. Toyama, H. Noda, T. Isobe, S. Takatori, T. Hiraki, H. Tatsuno, N. Kominato, M. Ito, Y. Sakai, H. Omamiuda, A. Yamaguchi, T. Yomogida, H. Miura, M. Nagasawa, S. Okada and Y. Takahashi, *Anal. Chim. Acta*, 2023, **1240**, 340755.
90 N. F. Chilton, R. P. Anderson, L. D. Turner, A. Soncini and K. S. Murray, *J. Comput. Chem.*, 2013, **34**, 1164–1175.
91 K. Katoh, B. K. Breedlove and M. Yamashita, *Chem. Sci.*, 2016, **7**, 4329–4340.
92 K. S. Cole and R. H. Cole, *J. Chem. Phys.*, 1941, **I**, 341–351.
93 A. Abragam and B. Bleaney, *Electron paramagnetic resonance of transition ions*, Oxford University Press, 2012.
94 A. Singh and K. N. Shrivastava, *Phys. Status Solidi*, 1979, **95**, 273–277.
95 A. Borah and R. Murugavel, *Coord. Chem. Rev.*, 2022, **453**, 214288.
96 J. K. Duchowski and D. F. Bocian, *J. Am. Chem. Soc.*, 1990, **112**, 3312–3318.
97 G. Liang, M. Croft, D. C. Johnston, N. Anbalagan and T. Mihalisin, *Phys. Rev. B: Condens. Matter Mater. Phys.*, 1988, **38**, 5302–5309.
98 H. A. Mook and R. M. Nicklow, *Phys. Rev. B: Condens. Matter Mater. Phys.*, 1979, **20**, 1656–1662.
99 The concept shown here was reported in the Grants-in-Aid for Scientific Research (C) (No. 21K05010) project in 2021. Principal Investigator: Dr Keiichi Katoh, Title: High-speed control of the magnetisation of single-molecule magnets via fluctuation of the valence state of rare earth elements. https://kaken.nii.ac.jp/grant/KAKENHI-PROJECT-21K05010/.
100 Y. Horii, M. Damjanović, M. R. Ajayakumar, K. Katoh, Y. Kitagawa, L. Chibotaru, L. Ungur, M. Mas-Torrent, W. Wernsdorfer, B. K. Breedlove, M. Enders, J. Veciana and M. Yamashita, *Chem. – Eur. J.*, 2020, **26**, 8621–8630.
101 K. Kobayashi, *Single-molecule magnet properties of light rare earth Ce(III) phthalocyaninato multiple-decker complexes*, M.Sc. Dissertation, Tohoku university, Japan, 2016.
102 Y. Horii, Y. Horie, K. Katoh, B. K. Breedlove and M. Yamashita, *Inorg. Chem.*, 2018, **2**, 565–574.
103 Y. Horii, K. Katoh, B. K. Breedlove and M. Yamashita, *Chem. Commun.*, 2017, **53**, 8561–8564.
104 T. Morita, M. Damjanović, K. Katoh, Y. Kitagawa, N. Yasuda, Y. Lan, W. Wernsdorfer, B. K. Breedlove, M. Enders and M. Yamashita, *J. Am. Chem. Soc.*, 2018, **140**, 2995–3007.
105 Y. Horii, S. Kishiue, M. Damjanović, K. Katoh, B. K. Breedlove, M. Enders and M. Yamashita, *Chem. – Eur. J.*, 2018, 4320–4327.
106 K. Katoh, N. Yasuda, M. Damjanović, W. Wernsdorfer, B. K. Breedlove and M. Yamashita, *Chem. – Eur. J.*, 2020, **26**, 4805–4815.

107 T. Sato, B. K. Breedlove, M. Yamashita and K. Katoh, *Angew. Chem., Int. Ed.*, 2021, **60**, 21179–21183.
108 A. G. Martynov, Y. Horii, K. Katoh, Y. Bian, J. Jiang, M. Yamashita and Y. G. Gorbunova, *Chem. Soc. Rev.*, 2022, **51**, 9262–9339.
109 A. A. Trifonov, I. A. Borovkov, E. A. Fedorova, G. K. Fukin, J. Larionova, N. O. Druzhkov and V. K. Cherkasov, *Chem. – Eur. J.*, 2007, **13**, 4981–4987.
110 I. L. Fedushkin, O. V. Maslova, A. G. Morozov, S. Dechert, S. Demeshko and F. Meyer, *Angew. Chem., Int. Ed.*, 2012, **51**, 10584–10587.
111 M. A. Hay and C. Boskovic, *Chem. – Eur. J.*, 2021, **27**, 3608–3637.
112 M. A. Dunstan, A. S. Manvell, N. J. Yutronkie, F. Aribot, J. Bendix, A. Rogalev and K. S. Pedersen, *Nat. Chem.*, 2024, **2**, 1–8.